THE ASTROPHYSICAL JOURNAL, 449:93–104, 1995 August 10

THE X-RAY ENVIRONMENT OF THE DUMBBELL RADIO GALAXY NGC 326

D. M. WORRALL, M. BIRKINSHAW, AND R. A. CAMERON
Harvard-Smithsonian Center for Astrophysics, 60 Garden Street, Cambridge, MA 02138
Received 1994 October 24; accepted 1995 February 22

ABSTRACT

We report the first detailed X-ray observations of the dumbbell radio galaxy NGC 326. The region containing the source was imaged for 5.8 hr in soft X-rays with the *ROSAT* PSPC as part of a program to measure the X-ray emission in low-power radio galaxies not known to be in rich clusters.

Unlike other radio galaxies measured as part of this program, NGC 326 is discovered to be embedded in bright asymmetrical X-ray–emitting cluster gas of temperature $kT \sim 2$ keV and 0.1–2.4 keV luminosity 3.5×10^{36} W ($H_0 = 50$ km s^{-1} Mpc^{-1}). There is a peak in the X-ray emission consistent with the location of the radio galaxy core. Five of the 10 brightest galaxies in the region are the brightest optical objects in error circles of excess X-ray emission. In the same observation, *ROSAT* also detected the unrelated, more distant, cluster Abell 115 and provided its first spectral measurement: $kT = 7.2^{+9}_{-1.9}$ keV.

It has been suggested previously that galaxy kinematics are responsible for the apparent change in direction over time of the twin jets of the large-scale radio emission of NGC 326. This was thought to be due either to a misalignment between the radio beam and galaxy axes or to interaction between the two galaxies which form the dumbell nucleus of NGC 326 and which are known to be passing at about 16 kpc projected separation. Our X-ray results support a different explanation: that buoyancy forces have bent the outer radio structure.

Subject headings: galaxies: clusters: individual (Abell 115) — galaxies: individual (NGC 326) — galaxies: jets — intergalactic medium — X-rays: galaxies

1. INTRODUCTION

The radio source B2 0055+26 (4C 26.03) was discovered by Colla et al. (1975) to be associated with the elliptical galaxy NGC 326 at a redshift of 0.047. The galaxy was subsequently found to have a double nucleus (Battistini et al. 1980). Wirth, Smarr, & Gallagher (1982) measured the projected separation of the galaxy centers to be 6″ and used the system to define the most elliptical class of dumbbell galaxy, db1.

The radio source was found by Ekers et al. (1978) to have an interesting structure: two curving tails with a 180° rotational symmetry (see Fig. 8 later in this paper). Nothing was known about the surrounding medium, and although NGC 326 is the brightest galaxy of Zw 0056.9+2636 (Zwicky & Kowal 1968), Ekers et al. described this as a small group and concluded that the shape of the radio source is determined by the central engine rather than the surrounding medium. They demonstrated that the observed structures could be produced if the radio beams are sweeping out cones on either side of the galaxy and have completed about a quarter of the rotation in the lifetime of the radio source. They suggested precession, due to a mismatch between the beam and galaxy axes, as the effect most likely to change the directions of the radio beams.

Wirth et al. (1982), knowing about the dumbbell nucleus, argued that the structure of the radio source had nothing to do with the central engine but was, instead, caused by a single change of direction of the radio beams during close passage between the two elliptical galaxies: beams which once pointed northeast and southwest had changed direction to point southeast and northwest. A change in the direction but not the amount of bending between the beams was suggested to indicate a change in the direction of the velocity vector of the system through the Zwicky cluster.

This paper presents for the first time detailed results on the structure of the intercluster medium surrounding NGC 326. We have discovered X-ray–emitting gas of cluster, rather than group, scale and density. Indeed, the source is unusual in being the only one so far in our X-ray study of low-power radio galaxies not known to be in rich clusters which shows such obvious cluster-scale hot gas (Worrall & Birkinshaw 1994, and work in preparation). Our results show that, contrary to previous work, the surrounding medium may be affecting the radio structures of the source.

2. X-RAY OBSERVATIONS AND ANALYSIS PROCEDURES

We observed NGC 326 with the *ROSAT* Position Sensitive Proportional Counter (PSPC; Trümper 1983; Pfeffermann et al. 1987) for 21 ks during 1992 July 24–29. The observation was made in "wobble" mode in order to permit correction for the obscuration caused by the window-support mesh. Here we expand the initial data analysis of Worrall & Birkinshaw (1994) by removing times of high background from the data, making background-subtracted, exposure-corrected images, contouring the images in a way which compensates for the statistical uncertainties and the fact that the point response worsens toward the edge of the field of view, and fitting spectral models to spatially selected regions.

Our data reduction was performed using the Post Reduction Off-line Software (PROS; Worrall et al. 1992) and other standard IRAF tasks. To remove intervals of high particle background we excluded times when the reading of the master veto rate (MVRATE) was greater than 170. We then looked at the resulting low-energy (0.2–0.7 keV) light curve extracted for regions away from X-ray sources to check for residual times of high background, particularly due to solar-scattered X-rays

which tend to be more predominant immediately before and after Earth occultations; none was found. The resulting X-ray event file had 19,409 s of acceptable data.

There was a slight change in roll angle during the set of observation intervals which make up the complete exposure. The first 59% of the exposure has a roll angle of ~ 194°.95–195°.05, the rest ~210°.90–211°.05. We were concerned that there may have been a change in the selection of aspect stars between these periods which may have resulted in the derived absolute positions (which can be in error by as much as 12″, 95% confidence; MPE 1992) being different between the two periods. We checked this by first analyzing the two periods separately, and we verified that sources do not shift relative to the aspect-corrected coordinate system; combined data were used for results presented in this paper.

We chose our background region to be a field-centered annulus of radii 7′.5–18′.75 and position angles 125°–290° and subtracted from it circles centered on sources found by Version 5.8 of the Standard Analysis Software System (SASS; Gruber 1992), which had been run prior to our receipt of the data. The radii of our excluded circles ranged between 2′ and 3′, depending on the relative strength of the source and its off-axis angle; 17 SASS sources overlapped our background region and were excluded. The average surface brightness in the resulting background region was 4.2×10^{-4} counts arcmin^{-2} s^{-1}, 0.2–2.3 keV.

The background over the field is expected to have a contribution due to particle events, which should be flat, and a contribution from stray X-rays, primarily solar scattered, which have been focused by the X-ray telescope and exhibit the same vignetting and obscuration as those of interest. We used an empirical approach to determine the relative contributions of these two sources of background to our data. To do this, we modeled the background over the whole field as a constant times the SASS exposure map plus an additional constant, and we used the data to determine the best values for the two constants. Following the method of Hughes & Birkinshaw (1995), the exposure map was first resampled onto 7″.5 square pixels, and our subsequent image analysis was performed using bins of this size. Best-fit values for the two constants were obtained using a radial profile through the source-subtracted background region (described above) in the exposure map and a similarly extracted profile (and errors) from the data. The best fit was statistically acceptable ($\chi^2 = 25.1$ for 28 degrees of freedom). The average surface brightness over the model background in the background region was 4.7×10^{-4} counts arcmin^{-2} s^{-1}, 0.2–2.3 keV. The fit gave ~20% of this surface brightness as nonvignetted, in good agreement with the particle background modeling of Snowden et al. (1992). The background-subtracted data were divided by a normalized version of the resampled exposure map to produce a surface brightness image for the 0.2–2.3 keV band. The whole procedure was repeated to produce an image for only the upper part of the energy range, 1–2.3 keV.

We used a modified version of the adaptive-smoothing procedure of Hughes & Birkinshaw (1995) to improve the contrast between point sources and diffuse emission in our background-subtracted, exposure-corrected images. First, because we were interested in data as far out as 32′ from the image center (where the point response of the telescope is as large as 160″ FWHM, and beyond the obscuring ring in the PSPC window-support structure at about 20′ radius), we smoothed the data by an amount which depended on the effective exposure time in the region. The image was split into four separate images based on the percentage of peak exposure: ≥91%, from ≥84% to <91%, from ≥70% to <84%, and <70%. Values in pixels not satisfying the condition were set to zero. These four images were then smoothed with Gaussians of $\sigma = 22''.5$, $37''.5$, 45″, and 60″, respectively. This meant that regions in the outer part of the image and those most obscured were smoothed by the greatest amount. A subsequent smoothing was then performed based on four bands of counts pixel^{-1} in the 0.2–2.3 keV image. The divisions (in units of counts arcmin^{-2} s^{-1}) were $\geq 3.1 \times 10^{-3}$, from $\geq 1.5 \times 10^{-3}$ to $< 3.1 \times 10^{-3}$, from $\geq 4.0 \times 10^{-4}$ to $< 1.5 \times 10^{-3}$, and $< 4.0 \times 10^{-4}$, and the sigmas of the Gaussians were 7″.5, 22″.5, 30″.0, and 112″.5, respectively. The hard-band (1–2.3 keV) image was then adaptively smoothed such that each pixel was smoothed by the same amount as its corresponding pixel in the broadband (0.2–2.3 keV) image, thus allowing subsequent comparison of the two smoothed images. The broadband image is shown in Figure 1.

3. SPATIAL STRUCTURE AND HARDNESS DISTRIBUTION OF THE X-RAY EMISSION

The PSPC data for the NGC 326 field exhibits diffuse emission in excess of background, filling a large portion of the region within the obscuring ribs of the window-support structure at a radius of ~20′ from the field center. The brightest peak in the central diffuse X-ray emission is coincident to within ~12″ with the radio core of NGC 326 at $0^h58^m22^s.63$, 26°51′58″.77 (J2000, 0″.1 error; E. Fomalont 1993, private communication). Because the source ~4′ to its east requires a similar position adjustment to improve the match with star SAO 74409 (the almost certain identification based on the relative X-ray and optical strengths of 9th magnitude F stars and on the fact that the associated X-ray emission is soft relative to the other X-ray emission in the field), we have shifted the coordinate frame of the X-ray field accordingly. Such a shift of ~12″ is within *ROSAT*'s absolute position errors (MPE 1992). Confirmation of the shift was later found by an excellent match of an X-ray source ~19′ northwest of NGC 326 with the position of star SAO 74389 (HD 5514, an 8th magnitude A star). With regard to establishing the reference frame it is unfortunate that the brightest star in the field, SAO 74405 (HD 5650, a K star of 7.5 mag), which is ~5′ south of NGC 326, was not detected in X-rays.

Figure 1 presents the background-subtracted, exposure-corrected, and adaptively smoothed 0.2–2.3 keV PSPC X-ray image, derived as described in § 2. NGC 326 is embedded in bright asymmetrical diffuse X-ray emission of full extent ≳800 kpc ($H_0 = 50$ km s^{-1} Mpc^{-1}) stretching predominantly northeast of the peak. The diffuse emission is of "cluster" rather than "group" scale, and we associate it with X-ray–emitting gas. Zw 0056.9+2636 (Zwicky & Kowal 1968) encompasses the region in which we detect X-ray emission but extends far to the south and east of the field shown in Figure 1. The area of the Zwicky cluster on the sky is ~1.4 deg^2, and it is described as medium compact, with a population of 145 galaxies brighter than a photographic magnitude of 15.7, and near ($z < 0.05$) by Zwicky & Kowal. Few redshifts are known for galaxies in the cluster, but those that are known range from $z = 0.017$ to $z = 0.047$ (de Vaucouleurs et al. 1991). This wide redshift range, a visual inspection of the Palomar Sky Survey plates, and the morphology of the X-ray emission suggest that cluster

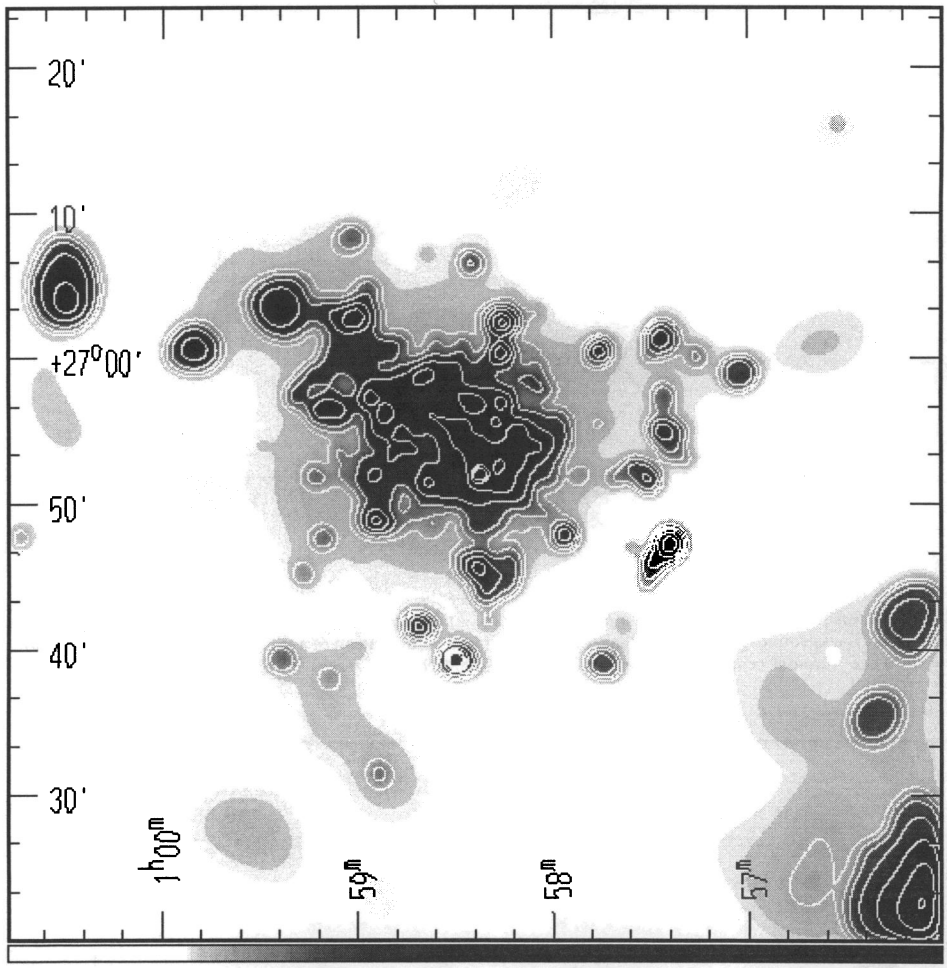

FIG. 1.—Background-subtracted, exposure-corrected, and adaptively smoothed 0.2–2.3 keV PSPC X-ray image. The axes show J2000 equatorial coordinates. Contour levels, in units of 10^{-3} counts arcmin^{-2} s^{-1}, are 0.18, 0.3, 0.5, 0.83, 1.4, 2.3, 3.9, and 6.6. NGC 326 is identified with the brightest peak in the diffuse emission at the center of the field. The X-ray emission which extends off the southwestern corner of the image is associated with the unrelated, more distant, cluster Abell 115. At the redshft of NGC 326, 10′ corresponds to 766 kpc for $H_0 = 50$ km s^{-1} Mpc^{-1}.

0056.9+2636 is a composite object, made up of two (or possibly three) poorer clusters.

Worrall & Birkinshaw (1994) extracted a radial profile about the maximum likelihood centroid of X-ray emission in NGC 326. Data for position angles 125°–290°, where the cluster gas extends the least, were used. Background was taken from an annulus of radii 3′–5.′7 within the same position angles. We used only counts for the energy band 0.2–1.9 keV, for which the PSPC point-response function (PRF) is well modeled. The background-subtracted radial profile was fit to a convolution of the energy-dependent PRF (weighted according to the spectral distribution of the data) with radially symmetric spatial models. Here we present the results of repeating this analysis using background from our carefully selected background region rather than from a region closer to the peak of the emission. Best-fit parameters were determined for a fit of the background-subtracted radial profile to an unresolved component, a β-model which is appropriate for gas in hydrostatic equilibrium (Cavaliere & Fusco-Femiano 1978; Sarazin 1986), and a combination of an unresolved component and a β-model. An unresolved component alone gives an unacceptable fit ($\chi^2 = 9780$ for 11 degrees of freedom), as might be expected from looking at Figure 1. A β-model alone gives a significantly worse fit than the combination of a β-model and an unresolved component. Figure 2 (*left*) plots χ^2 against core radius for different values of β. The dashed curves, for a β-model alone, all give an unacceptable minimum χ^2 (greater than 42 for 10 degrees of freedom). The fits to a joint β-model and unresolved component are all acceptable for $\beta \geq 0.5$. Such a value of β is consistent with values generally fit for cluster gas (see, e.g., Sarazin 1986). Our new fit for $\beta = \frac{2}{3}$ gives a core radius of $200'' \pm 13''$ (255 kpc), consistent with the value of $230'' \pm 30''$ fit by Worrall & Birkinshaw (1994) using a less precise measure of the background. Figure 2 (*right*) plots the background-subtracted radial profile and best fit for a two-component model with $\beta = 0.9$. There are 1066 net counts in the 0.2–1.9 keV profile, and the unresolved component contains 60 ± 10 counts.

Figure 3 shows the background-subtracted, exposure-corrected, adaptively smoothed hard X-ray image (1–2.3 keV), derived as described in § 2, divided by the broadband (0.2–2.3 keV) image of Figure 1. Only regions where both the hard and broadband data are above 20% of background have been used. The contours of Figure 1 are superimposed. The darkest regions on the image correspond to those with the hardest X-ray spectrum. The plot is particularly useful in indicating point sources which differ from the cluster gas in their spectrum. For example, the source 4′ to the east of the peak at

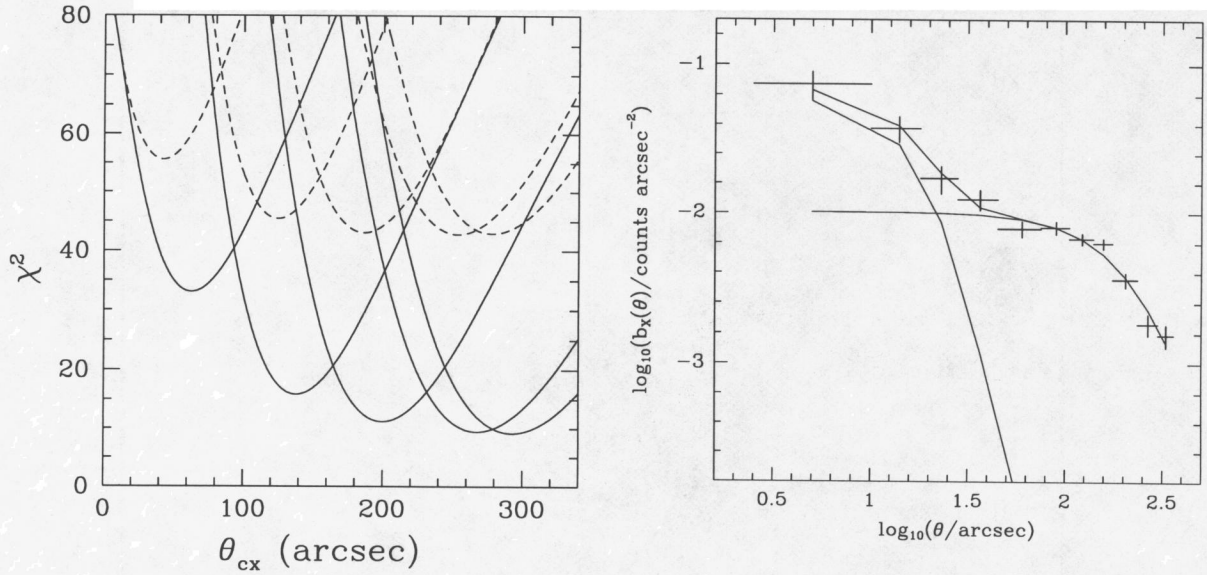

FIG. 2.—*Left*: χ^2 as a function of core radius, θ_{cx}, for a fit to the background-subtracted 0.2–1.9 keV radial profile for position angles 125°–290° centered on NGC 326, to a β-model (*dashed curves*) and the combination of a β-model and an unresolved source (*solid curves*). Each set of curves, from left to right, corresponds to $\beta = 0.35, 0.5, 0.6667, 0.9, 1.0$. *Right*: Background-subtracted radial profile and fit to a combination of a β-model and unresolved component for $\beta = 0.9$. $\chi^2 = 9.4$ for 9 degreees of freedom, $\theta_{cx} = 267''$, the β-model central brightness is 0.0107 ± 0.0004 counts arcsec^{-2}, and 60 ± 10 counts are in the unresolved component. The exposure time is 19,409 s.

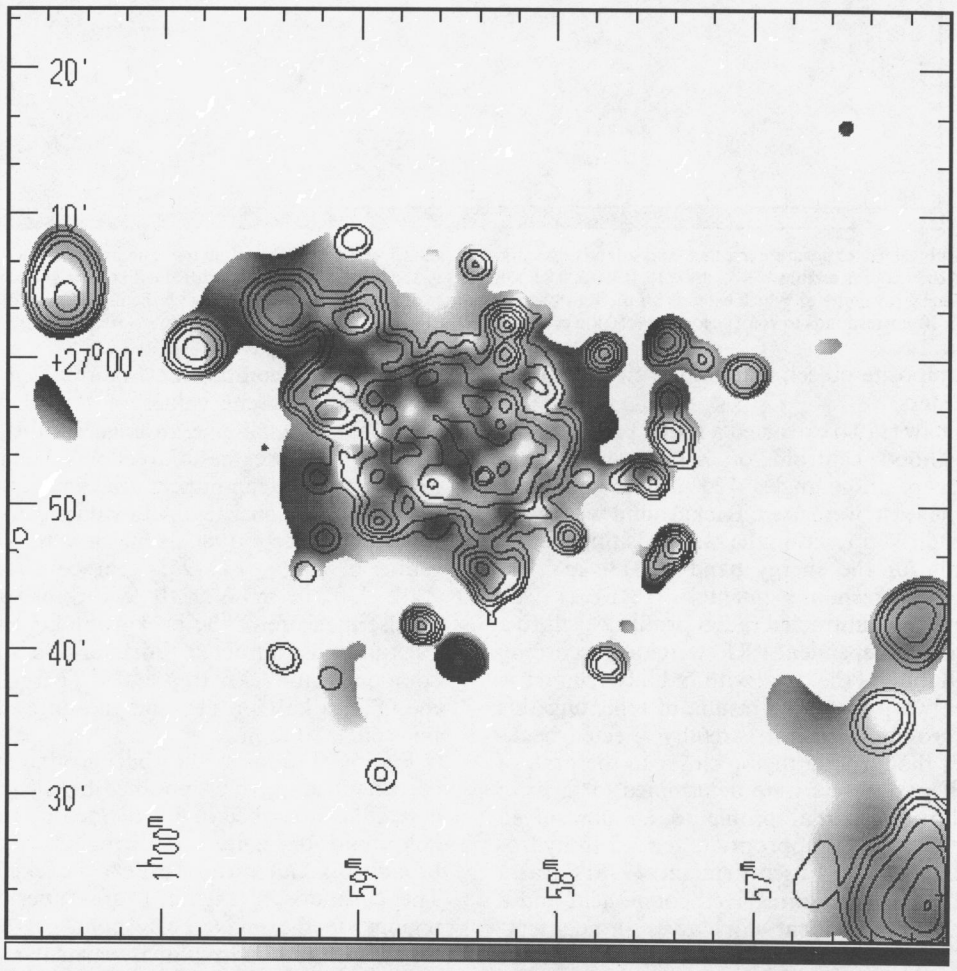

FIG. 3.—Background-subtracted, exposure-corrected, adaptively smoothed hard X-ray (1–2.3 keV) image divided by the broadband (0.2–2.3 keV) image, with the broadband contours of Fig. 1 superimposed. The darkest regions on the image correspond to those with the hardest X-ray spectrum.

NGC 326 has a relatively soft spectrum, supporting its identification with the star SAO 74409. Figure 3 also shows that the cluster gas shows no sign of being cooler at its outer extremeties.

4. OPTICAL CANDIDATES FOR THE X-RAY–EMITTING FEATURES

The image (Fig. 1) reveals many possible discrete X-ray sources which are either confused with the diffuse emission or lie outside it. It is of particular interest to determine if any of these possible X-ray emitters is associated with a galaxy at the cluster redshift. It is also interesting that Abell 115 lies off axis but fully within the complete field observed, and its spectrum and luminosity are reported in § 5.

In order to match galaxies with X-ray sources, we obtained from the Space Telescope Science Institute a file of the digitized, position-calibrated Palomar Observatory Sky Survey (POSS) data for the region of sky in our *ROSAT* image. Although NGC 326 is the brightest galaxy in the field, there are several other galaxies within ~ 3 mag. Visual inspection showed that the most prominent galaxies lie to the northeast of NGC 326 and are roughly co-extensive with the X-ray gas. This supports the argument that the diffuse X-ray emission is at the redshift of NGC 326, and not behind. Redshift measurements of the galaxies (see Table 1) are required for confirmation and to permit study of the hydrostatic state of the X-ray–emitting gas.

We have searched for coincidences between the galaxy positions and X-ray sources found by the SASS. SASS incorporates a sliding-box source detection algorithm followed by a maximum likelihood estimate of existence, flux, and position. Within the region of diffuse emission, SASS finds many overlapping sources in some regions. However, by taking only the 38 sources for the area shown in Figure 1 where the SASS maximum likelihood indicator of existence is greater than 40 for regions overlying the diffuse emission, and greater than 26 elsewhere, we find reasonable agreement with visual inspection of the data and with the detection algorithm available in PROS. We have added 12″ to the 1.4 σ positional uncertainties given by SASS in order to produce conservative radii for error circles of the X-ray sources, taking into account the possible residual aspect errors. Within a $\sim 20'$ radius circle of NGC 326 (1.5 Mpc projected distance), we find that five of the 10 brightest galaxies are the brightest optical objects in X-ray error circles (Table 1). This suggests that the galaxy atmospheres are not fully integrated into the cluster gas as a whole, with implications for the evolution of the cluster as a dynamical entity.

Our analysis of 1.4 GHz C-array VLA data for a field covering roughly the inner 70% of the area of Figure 1 (see § 7) finds a radio source of 105 ± 10 mJy consistent with the visually second-brightest galaxy, UGC 613; radio emission for the other galaxies in Table 1, with the exception of NGC 326, is $\lesssim 5$ mJy. Apart from the two galaxies NGC 326 and UGC 613, the only radio source which we have matched with an X-ray source lies within 5″ of $0^h57^m25^s.9$, 27°01′25″ and emits 78 ± 8 mJy; the digitized POSS reveals no obvious optical candidate.

5. ABELL 115

Abell 115 ($z = 0.197$) with optical position 0^h56^m, 26°19′ (J2000; Abell, Corwin, & Olowin 1989) was first detected in X-rays with the *Einstein Observatory*. The IPC image showed a double peak which Forman et al. (1981) suggested to be evidence for an intermediate stage in the evolution of the system, before final merger into a relaxed cluster. Subsequent optical work found three primary clumps of galaxies, two of which correspond to the X-ray peaks (Beers, Huchra, & Geller 1983). The brighter X-ray clump (the one to the north) contains the radio galaxy 3C 28, and Feretti et al. (1984), in a follow-up *Einstein Observatory* HRI observation, estimated that $\sim 30\%$ of the emission in the northern IPC peak could be associated with 3C 28 itself. The *Einstein Observatory* detections were weak (~ 200 net counts with the IPC and ~ 60 net counts with

TABLE 1

BRIGHTEST GALAXIES WITHIN $\sim 20'$ RADIUS OF NGC 326

Position[a] J2000 (to ~2″)	Name	X-Ray Detection[b] (yes/no)
$0^h58^m22^s.6$ 26°51′59″	NGC 326, Zw 0055.7+2636	Yes
0 59 24.5 27 03 33	UGC 613, Zw 0056.7+2647	Yes
0 59 03.6 27 02 33	MCG +04-03-030	Yes
0 58 47.5 26 58 40		No
0 58 04.4 26 53 47	MCG +04-03-024	Yes
0 58 28.5 26 53 43		No
0 59 00.4 27 08 47		Yes
0 58 09.6 26 48 00		No
0 58 49.0 27 00 12		No
0 59 16.4 26 52 02		No

NOTE.—Other galaxies (further from the field center, but in the magnitude range of those in the table) which may be X-ray emitters are three at $1^h0^m27^s.9$, 27°1′32″ (Zw 0057.8+2645, MCG +04-03-032), $1^h0^m34^s.1$, 27°5′53″ (MCG +04-03-033), and $1^h0^m31^s.4$, 27°4′27″, consistent with the contoured emission close to the left-hand axis in Fig. 1, and two at $0^h56^m45^s.4$, 27°0′35″ (MCG +04-03-021, UGC 585) and $0^h56^m41^s.9$, 27°1′39″, which are consistent with an apparent excess in Fig. 1 (just below the level of the contours and not found by the SASS detection algorithm).

[a] In order of decreasing magnitude estimated from visual inspection of the POSS. Positions use astrometry from the digitized POSS.

[b] Yes means coincidence of the galaxy with a SASS Version 5.8 X-ray error circle (see text). X-ray sources are listed in the SASS master source list, except for NGC 326 whose emission was combined with weaker surrounding "sources" and reported as a cluster.

the HRI) and unable to constrain the spectrum, which, on the basis of other clusters, was assumed to be from thermal gas of $kT \sim 6$ keV.

The long observing time and the increased sensitivity of *ROSAT* with respect to the *Einstein Observatory* renders a strong detection of Abell 115 (4870 ± 94 net counts 0.1–2.4 keV) despite the reduced sensitivity caused by its location 44′ off axis. We extracted a spectrum, measuring background from a region spanning the same off-axis annulus as Abell 115, but away from it and other contaminating sources. Our spectral fitting, which took into account the off-axis location of the source, confirms a relatively high temperature for the source. As shown in Figure 4, a single-temperature Raymond-Smith thermal model (Raymond & Smith 1977) gives a good fit ($\chi^2 = 28.8$ for 28 degrees of freedom) and finds $kT = 7.2^{+9}_{-1.9}$ keV (1 σ error for two interesting parameters; the PSPC is poor at constraining the upper limit to temperatures of hot gas because of its soft response). The abundance fraction is also poorly constrained since the temperature is high; solar abundances give the best fit. There is marginal evidence for some absorption in addition to the Galactic value of 5.1×10^{20} cm^{-2} (Stark et al. 1992), with a best-fit range of 1.8×10^{19} to 2.6×10^{20} cm^{-2}. However, such absorption is needed at less than 95% confidence and could be induced by the oversimplicity of our single-component model. We found no significant improvement to our fit when we added a second thermal or a power-law component, which implies that if 3C 28 has a very different spectrum from the cluster gas, it contributes $\lesssim 10\%$ of the total counts (probably not incompatible with the *Einstein Observatory* results). An interesting point is that the luminosity we measure is roughly double that inferred by Forman et al. 1981, presumably since much of the low surface brightness cluster emission was blended into the background in the IPC measurement. The total *ROSAT* luminosity is 1.6×10^{38} W (0.1–2.4 keV), and an extrapolation of the spectrum gives 10^{38} W (1–3 keV) and 2×10^{38} W (2–10 keV).

For the large off-axis angle (~44′) at which Abell 115 was measured with *ROSAT*, the best approximation of the asymmetric PRF to a Gaussian has a $\sigma \sim 105''$ (Hasinger et al. 1993). Thus the *ROSAT* beam is more than twice the size of the on-axis *Einstein* IPC point response for a source of this spectrum (Harnden et al. 1984). Consequently, *ROSAT* does not resolve the two nuclei seen with the IPC, although we note a general north-south elongation as expected from the IPC image, with the northern part being brighter than the southern part.

6. X-RAY SPECTRUM

The contiguous central region, where the emission is brighter than the fourth from lowest contour of Figure 1, and excluding a region of radius 1′.75 around the X-ray centroid associated with NGC 326 itself and 1′.63 around the (X-ray fainter) SAO star to its east, gives 1619 ± 56 net counts (0.1–2.4 keV) in 63.6 arcmin^2 (in 19,409 s), taking background from our standard background region. Spectra were fitted using the latest versions of the PSPC response matrix (No. 36) and effective-area calibration (No. 2.6) appropriate to the time at which NGC 326 was observed. The spectrum gives a good fit to a single-temperature Raymond-Smith thermal model. An iron abundance fraction less than solar is found: $0.3^{+0.3}_{-0.15}$, 1 σ errors for one interesting parameter, $\chi^2_{\rm min} = 11.9$ for 26 degrees

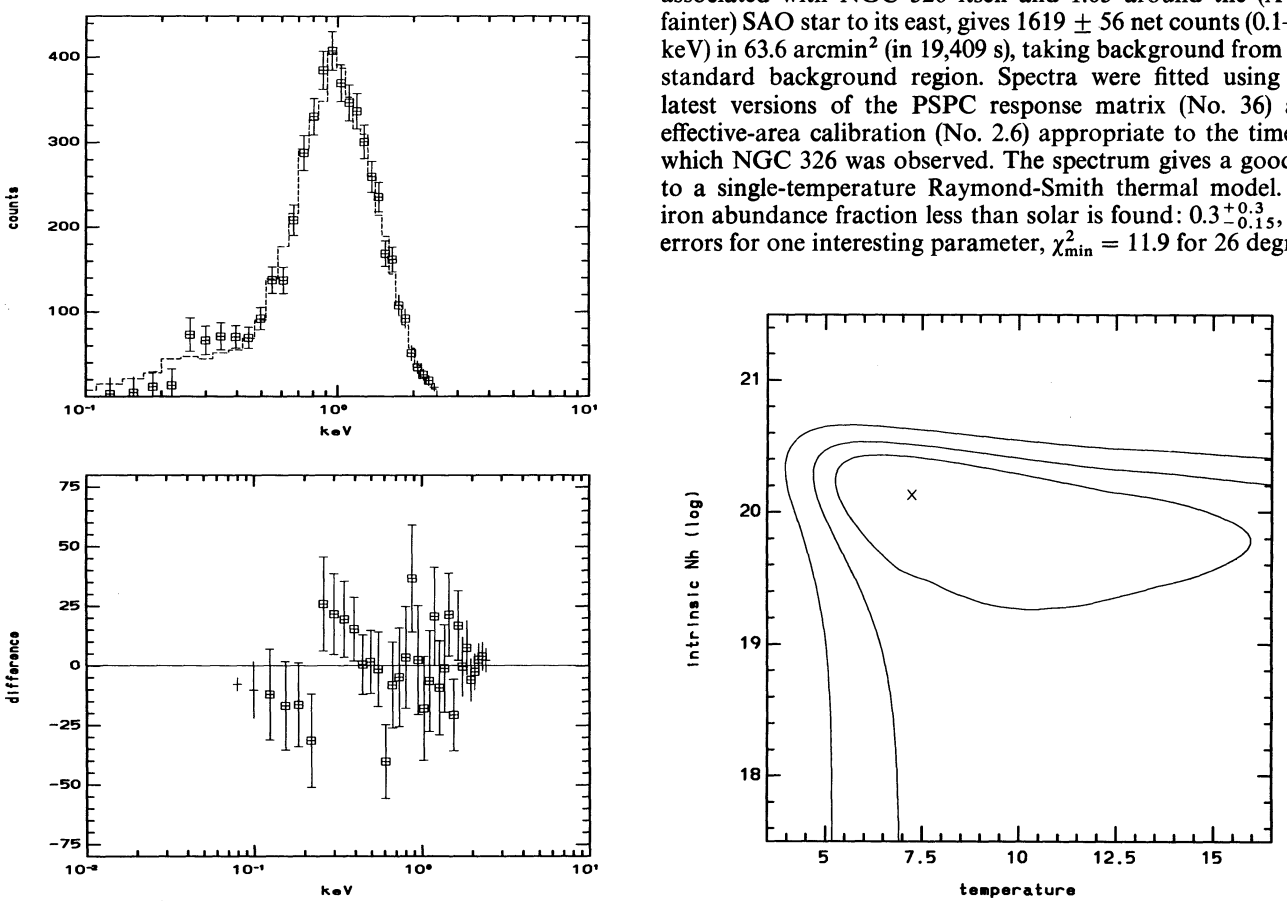

FIG. 4.—Spectral fit of the PSPC data for Abell 115 to a Raymond-Smith thermal model with 100% cosmic abundances and fixed Galactic $N_{\rm H}$ of 5.1×10^{20} cm^{-2}. The best-fit model ($\chi^2 = 28.8$ for 28 degrees of freedom) is for a temperature of $kT = 7.2$ keV and excess intrinsic absorption of 1.3×10^{20} cm^{-2}. Shown are net counts compared with model fit (*top left*), residuals (data − model) for the fit (*bottom left*), and contours of equal χ^2 at values of 2.3, 4.6, and 9.2 above the best-fit value, corresponding to uncertainties of 1 σ, 90%, and 99% for two interesting parameters (*right*).

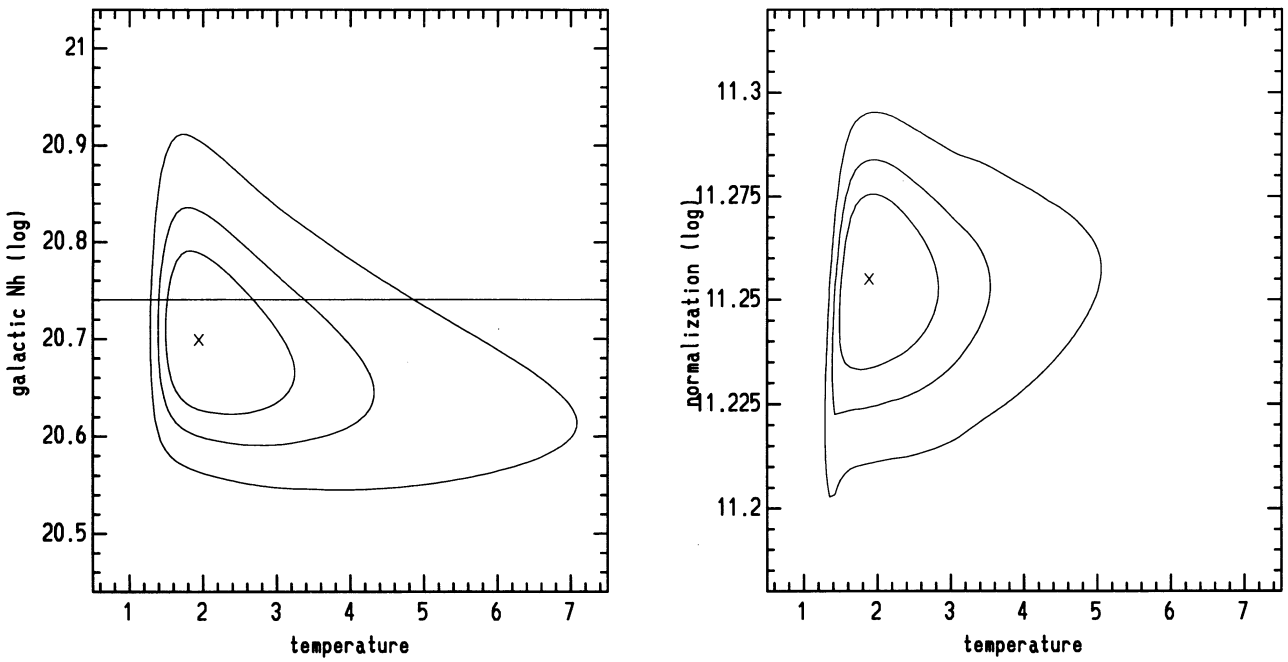

FIG. 5.—The χ^2 contours (1 σ, 90%, and 99% for two interesting parameters) for Raymond-Smith spectral fits to the diffuse emission in the contiguous 63.6 arcmin^2 central region where the emission is brighter than the fourth lowest contour on Fig. 1, and excluding a region around NGC 326 itself and the SAO star ~4′ to its east. The abundance fraction has been fixed at the best-fit value of 0.3. *Left*: Temperature, Galactic absorption, and normalization are free parameters. The plot shows good agreement with Galactic absorption from Stark et al. (1992), indicated with the horizontal line. *Right*: Absorption has been fixed at the Stark et al. (1992) value, and confidence contours are shown for the temperature (in units of kT) and the logarithm of the normalization (emission measure/$4\pi D^2$ in units of cm^{-5}).

of freedom. Such a result is in excellent agreement with the mean iron abundance of 0.35 ± 0.02 found by Arnaud et al. (1992) for clusters observed with *EXOSAT* and *Ginga*. Figure 5 (*left*) shows χ^2 contours (1 σ, 90%, and 99% for two interesting parameters) for temperature and Galactic absorption, assuming an abundance fraction of 0.3. The absorption is in excellent agreement with the Galactic absorption toward NGC 326 from Stark et al. (1992) of 5.5×10^{20} atoms cm^{-2}. Figure 5 (*right*) shows χ^2 contours of temperature versus emission measure/$4\pi D^2$ assuming an abundance fraction of 0.3 and that the only absorption is Galactic. Our conclusions are that the gas in this central region (not including the unresolved emission associated with NGC 326 itself) exhibits no absorption in excess of the Galactic value, has an abundance fraction less than solar, is of temperature $kT = 1.9^{+0.9}_{-0.4}$ keV, and has an emission measure/$4\pi D^2$ of $(1.80 \pm 0.09) \times 10^{11}$ cm^{-5} for an abundance fraction of 0.3. The luminosity, adopting the redshift of NGC 326 and $H_0 = 50$ km s^{-1} Mpc^{-1}, is 1.6×10^{36} W. A consideration of the uncertainty in abundance increases the allowed upper limit to the temperature slightly, to 3.2 keV. The emission measure/$4\pi D^2$ is dependent on abundance fraction, and for example, we find $(2.03 \pm 0.16) \times 10^{11}$ cm^{-5} for an abundance fraction of 0.1 and $(1.53 \pm 0.12) \times 10^{11}$ cm^{-5} for an abundance fraction of 0.6.

To estimate the total luminosity of gas we took all emission brighter than the lowest contour of Figure 1 and excluded circles around 38 discrete sources (see § 4). This gave 3673 ± 117 net counts in 293 arcmin^2. Despite the large area, the spectrum again gave an acceptable fit to a single-temperature thermal ($\chi^2 = 25.5$ for 26 degrees of freedom), with parameter values similar to those shown in Figure 5 (*left*). The 0.1–2.4 keV luminosity is 3.5×10^{36} W. When the spectrum is extrapolated to the energy range 2–10 keV, we find 10^{36} W, giving excellent agreement with the correlation of X-ray luminosity and temperature for clusters of David et al. (1993; see their Fig. 5*a*).

In order to get a better estimate of the temperature and emission measure of the gas in the vicinity of the radio lobes of NGC 326 (see Fig. 8 later in the paper), we repeated the procedure above using only the emission from a contiguous region in the center, brighter than the fifth from lowest contour of Figure 1. This time we excluded a region of radius only 45″ around the X-ray centroid of emission at NGC 326 itself; Figure 2 (*right*) shows that this radius is sufficient to exclude the region in which the unresolved component dominates. This central diffuse emission gives 635 ± 35 net counts (0.1–2.4 keV) in 17.2 arcmin^2. The best-fit abundance fraction is not significantly different from that found for the gas over the larger region, and contour plots equivalent to those of Figure 5 but for this smaller region of brighter central gas are shown in Figure 6. Like the gas on a larger scale, we find that the central gas exhibits no absorption in excess of the Galactic value and gives an excellent fit to a single-temperature thermal model. The temperature is $kT = 1.8^{+1.9}_{-0.5}$ keV, the luminosity is 6×10^{35} W, and the emission measure/$4\pi D^2$ is $6.9^{+0.6}_{-0.7} \times 10^{10}$ cm^{-5} for an abundance fraction of 0.3. The comparison between the data and best-fit model are shown in Figure 7.

Within a circle of radius 45″ centered on NGC 326, the unresolved X-ray component matches the contribution from diffuse emission, at roughly 60 counts each. The unresolved emission contributes less by a factor of ~2.4 in total counts and 1 keV flux density than estimated by Worrall & Birkinshaw (1994). The 60 net counts within the 45″ circle, using the inner region of diffuse emission fit in Figure 6 as the background, could be either power-law or thermal emission. In either case the 0.2–1.9 keV luminosity is about 4×10^{34} W,

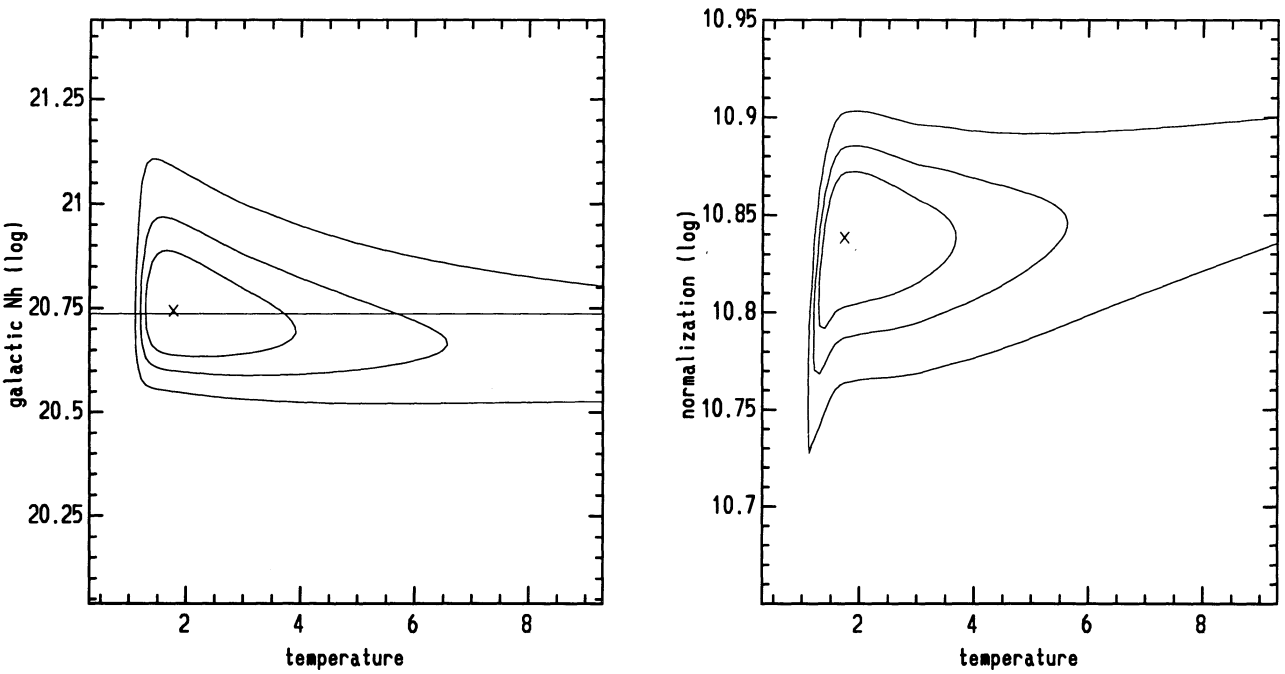

FIG. 6.—Same as Fig. 5, but for a contiguous 17.2 arcmin^2 region in the center where the emission is brighter than the fifth from lowest contour of Fig. 1, excluding a circle of radius 45″ which encompasses the unresolved X-ray emission from NGC 326 itself, as evident in Fig. 2*b*.

and the arguments of Worrall & Birkinshaw (1994) still hold: this is too large a luminosity to be dominated by the integrated emission of discrete X-ray sources similar to those in spiral galaxies.

A possible origin for the unresolved component is gas on a scale size less than or equal to that of the galaxy system, since this would be unresolved to the PSPC. Worrall & Birkinshaw (1994) have already shown that the cluster emission is cooling too slowly for a cooling flow to have been initiated. However, if the unresolved emission is hot gas, it would be cooling on a timescale shorter than the Hubble time.

An alternative origin for the unresolved component is non-thermal radiation from the active nucleus responsible for the radio jets. Our revised X-ray spectral luminosity of $(6 \pm 4) \times 10^{15}$ W Hz^{-1} sr^{-1} brings the source into agreement with the correlation of X-ray core and radio core components for low-power radio galaxies shown in Figure 2 of Worrall & Birkinshaw (1994).

7. RADIO DATA

Radio images of NGC 326 were obtained from the 5 GHz mapping survey of Birkinshaw & Davies (1995) and from the analysis of archival 1.4 GHz data taken by Parma, Cameron, & de Ruiter (1991). Figure 8 shows these images superimposed on a gray-scale representation of the X-ray emission near NGC 326.

The 5 GHz data used in Figure 8*a* were taken with the VLA in its C array on 1989 June 15 as a part of a galaxy imaging survey, and the map was constructed following standard reduction procedures (including self-calibration) and combining both intermediate frequencies (IFs). The central structure of the radio source is not clearly split into distinct jet and core

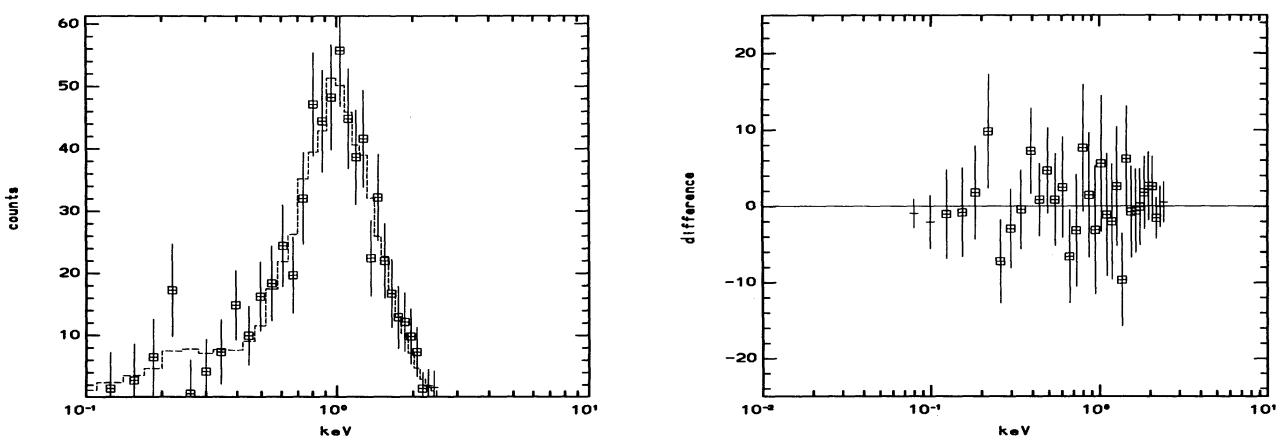

FIG. 7.—Net counts compared with best-fit model (*left*) and residuals (data − model; *right*) for data for which contours are shown in Fig. 6. The model is a Raymond-Smith thermal of $kT = 1.78$ keV, 30% cosmic abundances, and Galactic N_H ($\chi^2 = 14.1$ for 28 degrees of freedom).

1995ApJ...449...93W

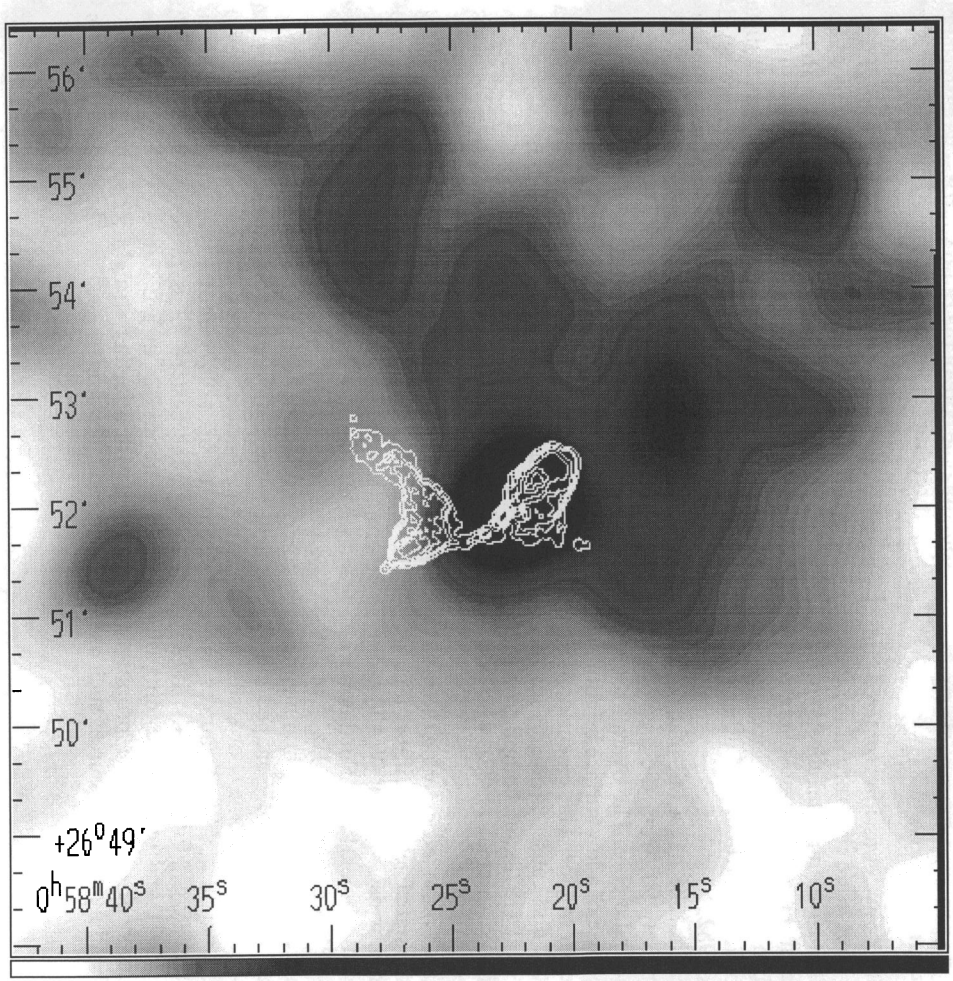

FIG. 8a

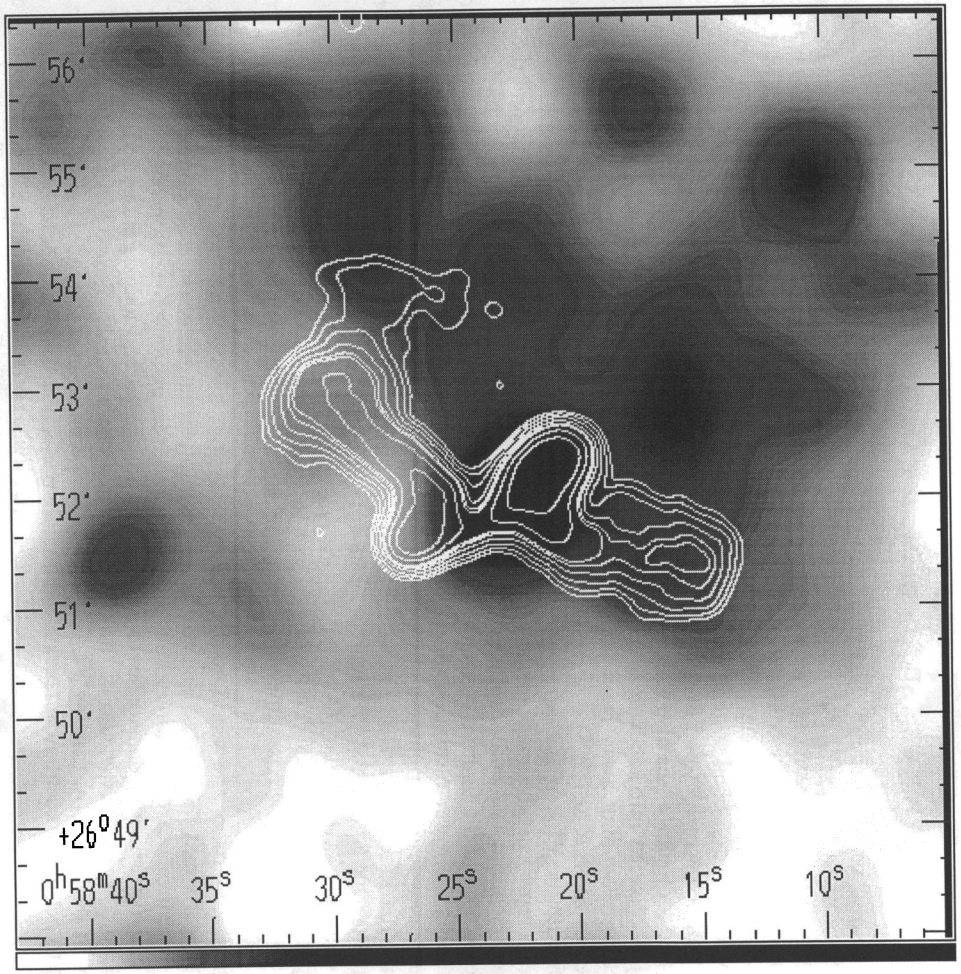

FIG. 8b

FIG. 8.—Gray-scale plots of the central region of the X-ray image, labeled with J2000 equatorial coordinates, with superimposed 5 GHz and 1.4 GHz VLA maps of NGC 326. The X-ray image shown here was constructed by a simple Gaussian smoothing (with $\sigma = 20''$) of the *ROSAT* PSPC image, so that the clumpy structure of the central emission is more evident than in Fig. 1. The unresolved X-ray source at $\sim 51'.5$ along the left-hand axis is coincident with star SAO 74409. (*a*) 5 GHz map of Birkinshaw & Davies (1995) appears as white contours on the X-ray gray scale. The synthesized beam is an elliptical Gaussian with FWHM $4''.1 \times 3''.6$, elongated in P.A. 1°. Contours are drawn at 0.2, 0.6, 1.0, 1.8, 3.0, 5.0, 7.0, and 9.0 mJy beam^{-1}. (*b*) 1.4 GHz map constructed from data used by Parma et al. (1991). The synthesized beam is a circular Gaussian with FWHM $14''$. Contours are drawn at 0.8, 1.6, 3.2, 6.4, 10, 13, 26, and 51 mJy beam^{-1}. At the redshift of NGC 326, $1'$ corresponds to 76.6 kpc for $H_0 = 50$ km s^{-1} Mpc^{-1}.

components by the ~4″ synthesized beam: however, higher resolution 5 GHz data have been analyzed by E. Fomalont (1993, private communication) and resolve the ambiguities of the central structure. The central radio emission consists of two compact (angular size <0.″4) components, associated with the two optical nuclei of the NGC 326 dumbbell system, and prominent, two-sided, knotty radio jets which extend from the brighter (northwestern) of the two radio cores (see also Parma et al. 1987). Further out, the jets broaden into lobes of emission, which have tailed structures extending away from the center of the galaxy, as described by Ekers et al. (1978).

The 1.4 GHz data were taken with the VLA in its C array on 1985 September 28, and Figure 8*b* represents the image formed by the usual analysis procedures (including self-calibration) for a single IF. The synthesized beam used in the figure is a circular Gaussian with FWHM 14″, and the lower resolution (due to the lower frequency) and increased source brightness (also due to the lower frequency) cause the 1.4 GHz map to be more sensitive to large-scale structure than the 5 GHz map of Figure 8*a*, despite the fact that both data sets have similar (C-array) antenna spacings. The total apparent 1.4 GHz flux density of NGC 326 in Figure 8*b* is 1.6 ± 0.1 Jy, which is somewhat smaller than the flux density of 1.75 Jy reported by White & Becker (1992) based on their analysis of the Condon & Broderick (1986) survey. This suggests that the map in Figure 8*b* is missing some large-scale structure: a careful examination of the data suggests that much of the missing flux density lies to the north of the galaxy center, in a western extension of the northeastern structure (at ~26°54′ decl.), but the existing VLA data are insufficiently extensive to permit an adequate image of this emission to be made.

8. INTERACTION OF THE RADIO STRUCTURES WITH THE X-RAY–EMITTING GAS

The presence of compact X-ray emission centered on NGC 326, and the symmetric large-scale structure of the radio source in NGC 326, suggests that environmental effects such as buoyancy of the radio plasma in the X-ray atmosphere could be involved in producing the bending of the radio lobes. Buoyancy has been invoked to explain the structure of other radio sources (e.g., Burns & Balonek 1982).

Figure 8 shows that each radio lobe has a tail that is bent through an angle of approximately 90° from the axis of the lobe, as defined by lines to the radio core. The overall source symmetry is broken by the presence of a low surface brightness extension of the tail from the eastern lobe. This extension is at an angle of about 90° to the tail and causes problems for the precessing-jet theory of Ekers et al. (1978) and complicates the dumbbell interaction theory of Wirth et al. (1982), who consider only the symmetric source structure.

Figure 8*a* shows well-collimated radio jets entering the radio lobes. The transition from collimated jets to diffuse tails is similar to such transitions seen in wide angle tail (WAT) radio sources (e.g., O'Donoghue, Owen, & Eilek 1990). Furthermore, the radio luminosity of NGC 326 (1.6×10^{25} W Hz^{-1} at 1.4 GHz) is within the narrow range of WAT radio luminosities observed by O'Donoghue et al. However, the Z-shaped morphology of NGC 326 is not compatible with the C or L shapes of WAT sources. The large-scale bending of WAT sources has long been difficult to explain (e.g., Eilek et al. 1984; O'Donoghue, Eilek, & Owen 1993), and buoyant bending of the lobes of NGC 326 is explored below. Another proposed explanation of the large-scale bending of radio sources such as WAT sources is the bulk motion of group gas containing the radio sources, for example due to an on-going merger of clusters of galaxies (Roettiger, Burns, & Loken 1993). In the case of NGC 326, the radio source symmetry argues more for galaxy-centered buoyancy effects than such random bulk motions in the cluster gas.

Here we consider the radio tails as part of the backflow from the radio lobes rather than markers of previous positions of the radio lobes. Numerical simulations of the lobes of classical double radio sources (e.g., Leahy & Williams 1984) show that material in the lobes flows back from the lobe hot spots. These simulations also show that the strength of the backflow depends on the relative densities of the jet and the surrounding medium, with light jets producing strong backflows and slow forward propagation of the front of the lobes. In NGC 326, the tails are at least 3 times longer than the lobe-core distances. If the lobes and tails are the same age and the jets have not changed orientation, then the flow velocities in the tails must be at least 3 times larger than the velocity of separation of the leading edges of the lobes from the radio core, suggesting light jets in NGC 326. As an indication of the actual backflow velocities, we use the results of Alexander & Leahy (1987) who used spectral index gradients in the radio lobes to infer separation velocities between the hot spot and lobe material in a representative sample of classical double radio sources. Most of these sources exhibit separation velocities between 0.01*c* and 0.2*c*. We lack spectral index gradient data for NGC 326, but might expect comparable flow velocities in its tails.

The superposition of the radio and X-ray data (Fig. 8) shows that, in projection, each radio lobe bends sideways into a tail as the backflow approaches the denser X-ray emission region surrounding the core of the radio source. The eastern tail bends so that it remains in a region of low X-ray brightness, and except for the low radio brightness extension of the tail, lies alongside the edge of a region of higher X-ray surface brightness. The low radio brightness extension, although superimposed on a region of brighter X-ray emission, does not conflict with the buoyancy force explanation of the radio structure. Being at the end of the eastern lobe, it may be at a considerable spatial distance from the X-ray emission region on which it is projected. The tail from the western lobe is superimposed on a region of higher X-ray brightness, but also points away from the X-ray emission surrounding the radio core.

In each tail, the bending has a radius of curvature of ~30″ (38 kpc). The bending of the eastern lobe occurs at ~45″ from the radio nucleus, as defined by the closest approach of the lobe to the nucleus, while the bending of the western lobe occurs at ~15″ from the nucleus. These bends are too close to the nucleus to be induced by pressure gradients associated with the extended X-ray component ($\theta_{cx} = 267''$) of the model shown in Figure 2. However, the bends could be produced by the smaller scale pressure gradients that are implied by a thermal origin for the compact component of the X-ray emission. Our data are consistent with a core radius for this component of up to ~15″. Such an X-ray core radius is comparable with both the radius of curvature of the bends and the distance of the bends from the radio and X-ray centers.

In the inner jet regions, the high-resolution radio image in Parma et al. (1987) shows straight symmetric inner jets, although the eastern jet is rather abruptly bent through an angle of about 32° at a distance of ~20″ (27 kpc) from the nucleus, with a further straight jet segment beyond the bend. No strong bending is seen in the shorter western jet. This

abrupt bending of the eastern jet is unlike the gradual bending seen in jets affected by ram pressure, as in NGC 1265 (O'Dea & Owen 1986). A brightening of the jet is associated with the abrupt bend: this may indicate a shock in the jet at this point. The lack of clear ram-pressure bending in the jets of NGC 326 indicates either that the galaxy is moving slowly relative to the surrounding X-ray atmosphere or that the jets are shielded by a galactic atmosphere from feeling any velocity-induced ram pressure. In what follows we will neglect ram-pressure effects in the analysis of the dynamics of the radio lobes and tails.

Minimum pressures in the radio tails are around 7×10^{-14} N m^{-2}, while the thermal pressure from the X-ray gas is 5×10^{-13} N m^{-2} at 60″ from the radio core, with the pressure from the extended X-ray component being the dominant contributor. This apparent pressure confinement of the radio lobes by the surrounding thermal material has been found in other low-power radio sources by Morganti et al. (1988), who suggest several possible explanations for the apparent pressure imbalance, including the deviation of internal lobe pressures from the minimum pressure, and entrainment of thermal material into the radio lobes. In NGC 326, the extended X-ray component shows a nonuniform, unrelaxed surface brightness structure, so that the radio lobes could be closer to pressure equilibrium than suggested by our simple model for the extended X-ray emission.

The dynamics of a buoyant radio source in a surrounding hot X-ray atmosphere are expressed by Euler's equation:

$$\frac{\partial \boldsymbol{v}}{\partial t} + (\boldsymbol{v} \cdot \nabla)\boldsymbol{v} = -\frac{\nabla P}{\rho_{\rm lobe}} + \boldsymbol{g}\,, \tag{1}$$

where $\boldsymbol{v}$ is the velocity of material in the radio lobes, which has density $\rho_{\rm lobe}$ and is subject to a pressure gradient (∇P) and gravity ($\boldsymbol{g}$). If the lobe backflow is assumed to be steady and to occur at a constant speed, v, and the compact X-ray source is assumed to arise from gas with density $\rho_x(r)$ in hydrostatic equilibrium, so that

$$\boldsymbol{g} = \frac{\nabla P}{\rho_x}\,, \tag{2}$$

equation (1) can be approximated as

$$\frac{v^2}{2R} \approx \left(\frac{1}{\rho_x} - \frac{1}{\rho_{\rm lobe}}\right)\frac{dP}{dr}\,, \tag{3}$$

which relates the radial pressure gradient to the radius of curvature, R, of the backflow in the lobes. Positive buoyancy at any radius corresponds to $\rho_x > \rho_{\rm lobe}$. We estimate both the pressure gradient and ρ_x from a β-model for the measured compact X-ray component, assuming a temperature of 0.6 keV as is reasonable for an elliptical galaxy of this type. We assume this compact component is produced by isothermal gas having a 15″ core radius. The density ρ_x and radial pressure gradient dP/dr are obtained from direct evaluation of the β-model at the apparent radial distances of 45″ and 15″ for the east and west lobes, respectively. If we assume that the observed (projected) radius of curvature is close to $R = 30''$ for both the east and west lobes, and assume a flow speed v, then we can solve for $\rho_x/\rho_{\rm lobe}$. Since we have no direct measurement of the backflow speed in NGC 326, we will use $v \sim 3000$ km s^{-1}, at the low end of the range obtained by Alexander & Leahy (1987). Table 2 gives the resultant X-ray densities, pressure gradients, and pressure contrasts for the lobes. We find $\rho_x/\rho_{\rm lobe} \simeq 40$ (east) and 25 (west). These derived density ratios would be even greater for backflow speeds greater than 3000 km s^{-1}, and the flow remains buoyant for all plausible temperatures. With density contrasts of the derived size or larger, all the observed lobe bending can be attributed to the action of buoyancy forces, and the flow remains buoyant even if a significant fraction of the compact X-ray emission is produced by unresolved nonthermal emission associated with the radio core (Worrall & Birkinshaw 1994).

TABLE 2

BUOYANCY MODEL

Lobe	East	West
Radial distance	45″, 57 kpc	15″, 19 kpc
ρ_x (kg m^{-3})	4.9×10^{-25}	2.5×10^{-24}
dP/dr (N m^{-2} kpc^{-1})	-1.9×10^{-15}	-1.6×10^{-14}
$\rho_x/\rho_{\rm lobe}$	40	25

The magnitudes of the buoyancy forces on the lobes fall by a factor of 2 from their values at the bends at distances of about 60″ (east) and 25″ (west) from the X-ray center and drop to zero at 300″ (east) and 100″ (west) if $\rho_{\rm lobe}$ is taken to be constant. Thus, although it is plausible that the lobes remain buoyant over the entire structure shown in Figure 8*b*, away from the bends the buoyancy forces drop rapidly.

Thus the structure of the diffuse radio emission seen in Figure 8*b* can be attributed to the effects of buoyancy, with the bends in the tails being driven by the density gradient in a compact gas component, and the low surface brightness extension of the eastern lobe occurring at neutral buoyancy. Further studies of the source are needed to set limits to the velocity of the backflow and test this interpretation.

9. SUMMARY

The basic result and conclusions of our work can be summarized as follows:

1. The X-ray emission in the vicinity of NGC 326 is predominantly diffuse, but there is an unresolved peak which is consistent in position with the dumbbell radio galaxy and which provides an excess 0.1–2.4 keV luminosity of $\sim 4 \times 10^{34}$ W.

2. The bright asymmetrical X-ray–emitting gas in which NGC 326 is embedded has full extent $\gtrsim 800$ kpc and luminosity 3.5×10^{36} W. It stretches predominantly northeast of the peak and is cospatial with the optically brightest galaxies in the field, which are associated with the western part of Zw 0056.9+2636.

3. A radial profile of the southern part of the X-ray emission, centered on NGC 326, shows that the diffuse component fits a β-model with $\beta \geq 0.5$, consistent with general findings for cluster gas.

4. The diffuse X-ray emission fits a Raymond-Smith spectral model with $kT = 1.9^{+0.9}_{-0.4}$ keV and an abundance fraction 0.3 times solar, in good agreement with other clusters of similar X-ray luminosity. The X-ray peak, unresolved with the PSPC and coincident with the radio galaxy core, may be due to cooler gas or to nonthermal emission associated with the active nucleus responsible for the radio jets.

5. Within a $\sim 20'$ radius circle of NGC 326 (1.5 Mpc projected distance), we find that five of the 10 brightest galaxies are the brightest optical objects in error circles of discrete X-ray sources. This suggests that the galaxy atmospheres are not fully

integrated into the cluster gas as a whole, with implications for the evolution of the cluster as a dynamical entity.

6. The unrelated cluster Abell 115 was detected as a strong extended source, 44′ off axis and unconfused with emission from the cluster surrounding NGC 326. A single-temperature Raymond-Smith thermal model fits the cluster data ($\sim$5000 net counts) and finds $kT = 7.2^{+9}_{-1.9}$ keV. The total luminosity, 1.6×10^{38} W (0.1–2.4 keV), is about twice that previously measured in a shallower observation with the *Einstein Observatory* IPC.

7. The Z-shaped structure of the radio emission of NGC 326 has been interpreted previously as either precession of the central beam (Ekers et al. 1978) or a change in direction of the beam (from northeast-southwest to southeast-northwest) during close passage with the companion elliptical galaxy (Wirth et al. 1982). Our X-ray results support a different explanation: that buoyancy forces have been bent the outer radio structures into directions of decreasing external gas pressure.

We are grateful to the referee, Jack Burns, for his thoughtful report and suggestions, to Jack Hughes, Stuart Daines, and Larry David for discussions concerning analysis procedures for extended *ROSAT* sources, to Ed Fomalont for the positions of radio components from his analysis of high-resolution VLA data, and to the GASP group of the Space Telescope Science Institute for a file of the digitized, position-calibrated Palomar Sky Survey data for the region of sky in our *ROSAT* image. Use was made of the NASA/IPAC Extragalactic Database (NED) which is operated by JPL, Caltech, under contract with NASA. This work was funded by NASA grant NAG 5-1882 and NASA contract NAS 8-39073.

REFERENCES

Abell, G. O., Corwin, H. G., Jr., & Olowin, R. P. 1989, ApJS, 70, 1
Alexander, P., & Leahy, J. P. 1987, MNRAS, 225, 1
Arnaud, M., Rothenflug, R., Boulade, O., Vigroux, L., & Vangioni-Flam, E. 1992, A&A, 254, 49
Battistini, P., Bònoli, F., Silvestro, S., Fanti, R., Gioia, I. M., & Giovannini, G. 1980, A&A, 85, 101
Beers, T. C., Huchra, J. P., & Geller, M. J. 1983, ApJ, 264, 356
Birkinshaw, M., & Davies, R. L. 1995, in preparation
Burns, J. O., & Balonek, T. J. 1982, ApJ, 263, 546
Cavaliere, A., & Fusco-Femiano, R. 1978, A&A, 70, 677
Colla, G., Fanti, C., Fanti, R., Gioia, I., Lari, C., Lequeux, J., Lucas, R., & Ulrich, M.-H. 1975, A&A, 38, 209
Condon, J. J., & Broderick, J. J. 1986, AJ, 91, 1051
David, L. P., Slyz, A., Jones, C., Forman, W., Vritilek, S. D., & Arnaud, K. A. 1993, ApJ, 412, 479
de Vaucouleurs, G., de Vaucouleurs, A., Corwin, H. G., Jr., Buta, R. J., Paturel, G., & Fouqué, P. 1991, Third Reference Catalogue of Bright Galaxies (New York: Springer)
Eilek, J. A., Burns, J. O., O'Dea, C. P., & Owen, F. N. 1984, ApJ, 278, 37
Ekers, R. D., Fanti, R., Lari, C., & Parma, P. 1978, Nature, 276, 588
Feretti, L., Gioia, I. M., Giovannini, G., Gregorini, L., & Padrielli, L. 1984, A&A, 139, 50
Forman, W., Bechtold, J., Blair, W., Giacconi, R., Van Speybroeck, L., & Jones, C. 1981, ApJ, 243, L133
Gruber, R. 1992, in Data Analysis in Astronomy IV, ed. V. Di Gesu et al. (New York: Plenum), 153
Harnden, F. R., Fabricant, D. G., Harris, D. E., & Schwarz, J. 1984, Smithsonian Astrophys. Obs. Spec. Rep., 393
Hasinger, G., Boese, G., Predehl, P., Turner, T. J., Yusaf, R., George, I. M., & Rohrbach, G. 1993, NASA/GSFC/OGIP Calibration Memo CAL/ROS/93-015
Hughes, J. P., & Birkinshaw, M. 1995, in preparation
Leahy, J. P., & Williams, A. G. 1984, MNRAS, 210, 929
MPE (Max-Planck-Institut für Extraterrestrische Physik). 1992, *ROSAT* News, 10 (available from legacy.gsfc.nasa.gov)
Morganti, R., Fanti, R., Gioia, I. M., Harris, D. E., Parma, P., & de Ruiter, H. 1988, A&A, 189, 11
O'Dea, C. P., & Owen, F. N. 1986, ApJ, 301, 841
O'Donoghue, A. A., Eilek, J. A., & Owen, F. N. 1993, ApJ, 408, 428
O'Donoghue, A. A., Owen, F. N., & Eilek, J. A. 1990, ApJS, 72, 75
Parma, P., Cameron, R. A., & de Ruiter, H. R. 1991, AJ, 102, 1960
Parma, P., Fanti, C., Fanti, R., Morganti, R., & de Ruiter, H. R. 1987, A&A, 181, 244
Pfeffermann, E., et al. 1987, Proc. SPIE, 733, 519
Raymond, J. C., & Smith, B. W. 1977, ApJS, 35, 419
Roettiger, K., Burns, J., & Loken, C. 1993, ApJ, 407, L53
Sarazin, C. L. 1986, Rev. Mod. Phys., 58, 1
Snowden, S. L., Plucinsky, P. P., Briel, U., Hasinger, G., & Pfeffermann, E. 1992, ApJ, 393, 819
Stark, A. A., Gammie, C. F., Wilson, R. W., Bally, J., Linke, R. A., Heiles, C., & Hurwitz, M. 1992, ApJS, 79, 77
Trümper, J. 1983, Adv. Space Res., 2, 241
White, R. L., & Becker, R. H. 1992, ApJS, 79, 331
Wirth, A., Smarr, L., & Gallagher, J. S. 1982, AJ, 87, 602
Worrall, D. M., & Birkinshaw, M. 1994, ApJ, 427, 134
Worrall, D. M., et al. 1992, in Data Analysis in Astronomy IV, ed. V. Di Gesu et al. (New York: Plenum), 145
Zwicky, F., & Kowal, C. T. 1968, Catalogue of Galaxies and Clusters of Galaxies, Vol. 6 (Pasadena: Caltech)